Simulation of uranium dioxide polymorphs and their phase transitions

Paul C. M. Fossati,[*] Laurent Van Brutzel, and Alain Chartier

CEA, DEN, DPC, SCCME, Laboratoire de Modélisation de Thermodynamique et de Thermochimie, F-91191 Gif-sur-Yvette Cedex, France

Jean-Paul Crocombette

CEA, DEN, DMN, Service de Recherches de Métallurgie Physique, F-91191 Gif-sur-Yvette Cedex, France

In this article first-principles DFT calculations and molecular dynamics simulations using empirical potentials have been used to study four different polymorphs of uranium dioxide that appear under high compressive and tensile deformations. It has been found, as expected, that the ground-state structure is the fluorite-type structure (space group $Fm\bar{3}m$). Under high compressive deformation urania transforms into cotunnite-type structure (space group $Pnma$), as already known experimentally. The calculated transition pressure is 28 GPa in agreement with the experimental data. Under tensile deformation urania transforms into either scrutinyite-type structure (space group $Pbcn$) or rutile-type (space group $P4_2/mnm$) structure. These two phases are almost energetically degenerate; hence it is impossible to distinguish which phase is the most favorable. The transition pressure for both phases is found to be equal to -10 GPa. Subsequently, assessment of four of the most used empirical potentials for UO_2—Morelon, Arima, Basak, and Yakub—have been carried out comparing the equations of state with those found with DFT calculations. The Morelon potential has been found to be the most accurate to describe the different urania polymorphs. Using this empirical potential and a dedicated minimization procedure, complete transition pathways between the ground state ($Fm\bar{3}m$) and both tensile structures ($Pbcn$ or $P4_2/mnm$) are described. Finally, uniaxial tensile load molecular dynamics simulations have been performed. It has been found that for load in the $\langle 100 \rangle$ direction urania transforms into the $Pbcn$ structure while for load in the $\langle 110 \rangle$ direction it transits towards the $P4_2/mnm$ structure.

PACS number(s): 61.72.Cc, 61.80.Az, 66.30.hd

I. INTRODUCTION

Many compounds are naturally found in a fluorite-like structure (space group $Fm\bar{3}m$). Uranium dioxide in particular (UO_2) is a well-known example of an ionic crystal having a fluorite-like ground structure. It is also of very significant interest because of its use in the nuclear industry. Indeed some of its thermophysical properties such as high melting point, low thermal conductivity, and high resistance under irradiation make it a good nuclear fuel, used in nuclear power plants around the world. The conditions in nuclear reactors cause high thermal gradients, formation of point and extended defects, and fission gas accumulation. These defects cause high local stresses, which can induce local phase transitions and crack initiation. Therefore, in order to predict nuclear fuel degradation, it is crucial to have a fundamental understanding of its structural behavior. One important part of this behavior is how the crystal structure changes with deformation, that is, the different UO_2 polymorphs, their relative stability, and the ways they turn into each other.

Under pressure, other crystals with the $Fm\bar{3}m$ structure undergo a transition to the orthorhombic cotunnite structure (space group $Pnma$).[1] This transition has been confirmed with both experimental[2,3] and theoretical[4,5] studies in the case of UO_2.

Under tensile load, experimental works and MD simulations of ceria (CeO_2) nanorod, another oxide compound with $Fm\bar{3}m$ ground structure, exhibited a phase transition from fluorite-type to rutile-type structure (space group $P4_2/mnm$).[6] In UO_2, a transition from cubic to orthorhombic scrutinyite-type structure (space group $Pbcn$) has been found by Desai *et al.* using first-principles DFT calculations and molecular

dynamics (MD) simulations at the vicinity of grain boundaries, which play the role of stress concentrators.[7,8] Zhang *et al.* have also observed similar transformations in the fracture process zone during crack propagation in UO_2 using MD simulations.[9] These local phase transformations appear at the vicinity of the crack front before the creation of free surfaces as shown in Fig. 1. This figure is the result of a MD crack simulation in which a uniaxial tensile strain was applied along the $\langle 110 \rangle$ axis.[10] However, these transitions under tensile load have not been observed experimentally, probably because of the metastable character or the small size of the secondary phases. Although these studies are focused on UO_2, a lot of compounds undergo similar transitions.[11]

In spite of all these studies, we still lack a complete understanding on the structural changes that occur in UO_2 under deformation. Therefore, the aim of this study is to describe using DFT calculations and MD simulations the behavior of the four UO_2 polymorphs found previously (i.e., $Fm\bar{3}m$, $Pnma$, $P4_2/mnm$, and $Pbcn$) under either compressive or tensile load, as well as the phase transition mechanisms involved. For the MD simulation, we also assessed four of the most used empirical potentials for UO_2: Morelon,[12] Arima,[13] Basak,[14] and Yakub.[15]

This assessment is important for the interpretation of larger scale simulations that cannot be done currently using DFT models, such as irradiation events, crack propagation, and dislocations. It also helps ensure the phenomena are physically relevant, and not potential-dependent.

These models were used to calculate the energy-volume relations for the polymorphs as well as the thermodynamic transition pressures. The results were compared to the available data when possible. We found in particular that the Morelon
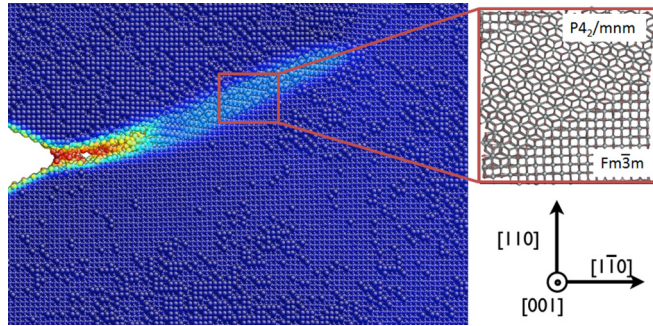
FIG. 1. (Color online) Crack propagation simulation snapshot showing a local phase transition ahead of the crack front. The loading is a uniaxial tensile strain applied along a ⟨110⟩ axis. The atoms are color coded according their potential energy. The secondary phase is denoted by light blue, whereas the bulk is in dark blue, and the advancing crack surface in orange/red. The encapsulated picture on the right is a zoom of the area including both fluorite structure and secondary phase. The printed axes show the crystallographic directions in the initial $Fm\bar{3}m$ structure.

potential gives the best agreement with both available experimental data and DFT calculations. For this reason, we used it in further investigations of the phase transitions. To this intent, we have developed a procedure to follow the pathway from one structure to another, and obtain a complete overview of the structural transformation without imposing a predetermined transition trajectory. These trajectories give a good description of the transitions in terms of symmetry elements and internal and external parameters change. However they are not sufficient in the sense that the nucleation process and the effects of the interfaces between the ground and secondary phases are important, especially at smaller length scales. They also lack a dynamic description of the phase transitions. For these reasons, we finally carried out finite-temperature MD simulations of the tensile phase transitions.

The paper is organized as follows: In Sec. II, the different crystal structures studied herein are described. In Sec. III,

we present a description of the computational methods used and the four empirical potentials. Section IV describes the results obtained on the stability of the different polymorphs and the transition pathways respectively. In the last section some conclusions are drawn.

II. STRUCTURAL ASPECTS

In the following, we describe the crystal structures of the five UO_2 polymorphs studied herein, i.e., $Fm\bar{3}m$, $Pnma$, $Pbcn$, $P4_2/mnm$, and $Pnnm$. In order to achieve a comprehensive description of the phase transitions, we also describe the crystallographic links between these structures.

The ground-state structure of UO_2 is known to be the fluorite-type structure. It can be described by the $Fm\bar{3}m$ space group, with the uranium ions setting in the 4a (0, 0, 0) special site and the oxygen ions setting in the 8c ($\frac{1}{4}$, $\frac{1}{4}$, $\frac{1}{4}$) special site (see Table I). This structure is composed of a face-centered cubic uranium sublattice, in which the oxygen ions occupy the tetrahedral sites, forming a simple cubic sublattice as illustrated in Fig. 2(a). Each uranium ion is coordinated to eight oxygen ions while each oxygen ion is tetrahedrally coordinated to four uranium ions.

The cotunnite structure is orthorhombic and is illustrated in Fig. 2(b). It appears under high pressure and is described in the $Pnma$ space group. Both oxygen and uranium ions sit in the 4c (x, $\frac{1}{4}$, z) special site, with different values for the internal parameters x and z. In particular, there are two sets of (x,z) values for the oxygen ions to achieve stoichiometry (see Table I), since the site multiplicity is the same for the oxygen and for the uranium ions. Compared to $Fm\bar{3}m$, the $Pnma$ structure exhibits a higher coordination number of 9 for uranium ions. The oxygen ions form elongated tricapped trigonal prisms that contain the uranium ions. The links between the $Fm\bar{3}m$ and the $Pnma$ structures rely on the 45° rotation of the (ab) plane and on an origin shift of ($\frac{1}{4}$, $\frac{1}{4}$, $\frac{1}{2}$). Therefore, the relations between the cell parameter lengths are $a_{Pnma} = \sqrt{2}a_{Fm\bar{3}m}$, $b_{Pnma} = a_{Fm\bar{3}m}/\sqrt{2}$, and $c_{Pnma} = a_{Fm\bar{3}m}$. The internal parameter of the uranium ions in the 4c special site must be $x = \frac{1}{4}$ and $y = \frac{1}{2}$.

TABLE I. Structural data for the different UO_2 crystalline structures studied herein. The values of the cell parameters and the internal fractional coordinates are averaged over the four potentials studied. The values for the $Pnnm$ structure have been extracted from the transition pathway (see Fig. 6) around 47 Å³/UO_2, close to the $P4_2/mnm$ structure. These values have been calculated with the Morelon potential only.

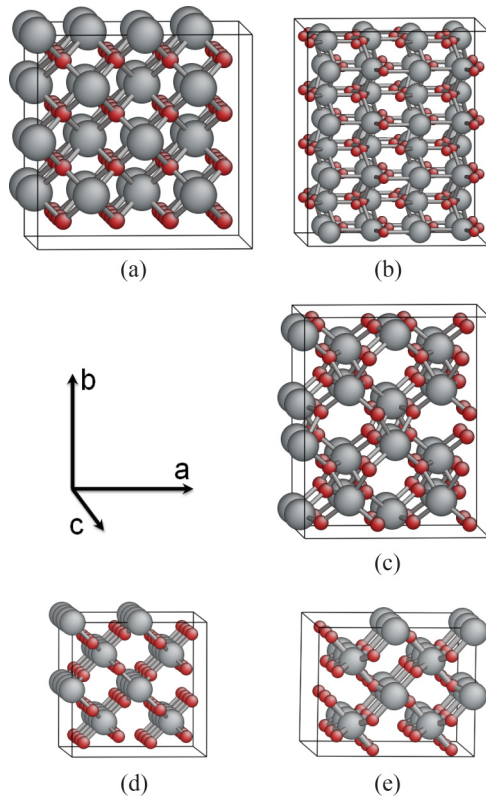| Name	Fluorite	Rutile	Marcasite	Scrutinyite	Cotunnite
Lattice system	cubic	tetragonal	orthorhombic	orthorhombic	orthorhombic
Space group (number)	$Fm\bar{3}m$ (No. 225)	$P4_2/mnm$ (No. 136)	$Pnnm$(No. 58)	$Pbcn$ (No. 60)	$Pnma$ (No. 62)
atoms/cell	12	6	6	12	12
Cell parameters (Å)	$a = 5.45 \pm 0.02$	$a = b = 5.15 \pm 0.03$ $c = 3.53 \pm 0.03$	$a = 5.225$ $b = 4.860$ $c = 3.713$	$a = 5.18 \pm 0.05$ $b = 6.12 \pm 0.08$ $c = 5.70 \pm 0.08$	$a = 6.01 \pm 0.01$ $b = 3.62 \pm 0.01$ $c = 7.02 \pm 0.04$
Uranium ions	4a (0, 0, 0)	2a (0, 0, 0)	2c (0, $\frac{1}{2}$, 0)	4c (0, y, $\frac{1}{4}$) $y = 0.174 \pm 0.001$	4c (x, $\frac{1}{4}$, z) $x = 0.254 \pm 0.001$ $z = 0.595 \pm 0.001$
Oxygen ions	8c ($\frac{1}{4}$, $\frac{1}{4}$, $\frac{1}{4}$)	4f (x, x, 0) $x = 0.3061 \pm 0.001$	4g (x, y, 0) $x = 0.2049$ $y = 0.1728$	8d (x,y,z) $x = 0.272 \pm 0.001$ $y = 0.394 \pm 0.001$ $z = 0.4226 \pm 0.0002$	4c (x, $\frac{1}{4}$, z) $x_{O_1} = 0.15 \pm 0.001$ $z_{O_1} = 0.93 \pm 0.001$ $x_{O_2} = 0.05 \pm 0.001$ $z_{O_2} = 0.33 \pm 0.001$

FIG. 2. (Color online) Atomic structures of the UO_2 polymorphs studied herein: (a) $Fm\bar{3}m$ (fluorite), (b) $Pnma$ (cotunnite), (c) $Pbcn$ (scrutinyite), (d) $P4_2/mnm$ (rutile), and (e) $Pnnm$ (marcasite). The uranium ions are represented by the large spheres and the oxygen ions by the small ones (respectively gray and red). The visible bonds link the U atoms to their first O neighbors.

The scrutinyite structure is more commonly known as the α-PbO$_2$ structure [see Fig. 2(c)]. It is orthorhombic and is described in the $Pbcn$ space group (see Table I). The uranium ions are in the 4c $(0, y, \frac{1}{4})$ special site and the oxygen ions sit in the 8d (x, y, z) special site. The coordination number of uranium is 6, lower than the one in the $Fm\bar{3}m$ structure. The UO_6 octahedra form planar chains sharing edges in a zigzag arrangement along the c direction. Each octahedron is strongly distorted, with the uranium being off-center. The key differences between the $Fm\bar{3}m$ and the $Pbcn$ structures are the elongation along the $\langle 010 \rangle$ direction and an origin shift of $(0, 0, \frac{1}{4})$. The $Fm\bar{3}m$ structure can be described in the same setting as the $Pbcn$ structure. The difference is that for the $Fm\bar{3}m$ structure the three axis lengths must be all equal. For the $Fm\bar{3}m$ structure, the uranium ions stay in the 4c special site but with $y = 0$, while the oxygen ions sit in the 8d special site with $x = y = z = \frac{1}{4}$.

The rutile structure is tetragonal and is described in the $P4_2/mnm$ space group. The uranium and oxygen ions set in the 2a $(0, 0, 0)$ and 4f $(x, x, 0)$ special sites, respectively (see Table I). Interestingly, the uranium sublattice is face-centered cubic type similarly to the $Fm\bar{3}m$ structure. The coordination number is 6 as seen in the $Pbcn$ structure. The octahedra share the edges of their basal planes along the c axis. These octahedral chains are linked to one another by corner sharing,

forming small tunnels along the c axis, as illustrated in Fig. 2(d).

The marcasite structure is described in the $Pnnm$ space group, with the uranium and oxygen ions setting in the 2c $(0, \frac{1}{2}, 0)$ and 4g $(x, y, 0)$ special sites, respectively. This structure, which has not been yet mentioned, is closely related to $P4_2/mnm$, and appears during some phase transitions, as will be shown later. It has an orthorhombic cell and a face-centered cubic uranium sublattice. The coordination number of uranium ions is 6 (forming UO_6 octahedra) like in the $P4_2/mnm$ structure, with rather similar arrangements between the octahedra. The most striking difference between both structures is a small rotation of the UO_6 octahedra around the c axis. The conventional cell of the $Fm\bar{3}m$ structure is related to the $Pnnm$ structure through a 45° rotation of the $Pnnm$ (*bc*) plane and an origin shift of $(0, \frac{1}{2}, 0)$. The relations between the cell parameter lengths of the $Fm\bar{3}m$ and the $Pnnm$ structures are written as follows: $a_{Pnnm} = a_{Fm\bar{3}m}$ and $b_{Pnnm} = c_{Pnnm} = a_{Fm\bar{3}m}/\sqrt{2}$. The uranium ions stay in the 2c $(0, \frac{1}{2}, 0)$ special site and the oxygen ions have $x = \frac{1}{4}$ and $y = 0$ in the 4g $(x, y, 0)$ special site. The $Pnnm$ and the $P4_2/mnm$ structures share the same cell axes and all the angles are equal to 90°. The $P4_2/mnm$ structure can be described as a particular $Pnnm$ structure, with $a_{Pnnm} = b_{Pnnm} = a_{P4_2/mnm} = b_{P4_2/mnm}$ and $c_{Pnnm} = c_{P4_2/mnm}$ and with an origin shift of $(0, \frac{1}{2}, 0)$. The internal parameters of the oxygen ions, x and y, have to be equal in order to describe the $P4_2/mnm$ structure.

III. COMPUTATIONAL DETAILS

To study the phase transitions in high pressure and tensile domains, we have performed two types of calculation. First-principles calculations were used in order to investigate with required accuracy the equations of state of the above-mentioned urania structures. Static calculations and MD simulations using empirical potentials were used to investigate detailed pathways of urania pressure-induced transitions because they are computationally less expensive. In the following section, we will describe both methods.

A. First-principles method

First-principles DFT calculations were performed using the ABINIT code[16] in the projector augmented wave formalism. The atomic data are identical to those used in the study of defects in UO_2.[17] Electron exchange and correlations were described by a generalized gradient approximation (GGA) functional of the Perdew-Burke-Ernzerhof type.[18] With this choice of functional we avoid the severe difficulties that appear when one uses "beyond local" functional (such as hybrid functional or local density approximation, LDA + U) due to the occurrence in such calculations of multiple minima that requires special care in the search for the ground state. Schemes have been proposed to solve the local minima problem, like occupancy matrix control[19,20] or U-ramping.[21] These schemes are very expensive from a computational point of view. Moreover, the lack of data about the secondary phases makes it hard to evaluate the improvements they would have over a simpler approach.

Even if one cannot reproduce the insulating nature of UO_2 with such "simple" GGA functional, they have proven able to

TABLE II. Parameters for the potential of Eq. (1).

| | Q | | A (eV) | | | ρ (Å) | | | C (eV Å^6) | D (eV) | B (Å^{-1}) | r_c (Å) |
	U	O	U-U	U-O	O-O	U-U	U-O	O-O	O-O	U-O	U-O	U-O
Morelon[12]	3.227552	−1.613626	0	566.49	11272.6		0.4202	0.1363	134	0	0	0
Arima[13]	2.7	−1.35	2.48128×10^{13}	55911.95	979.057	0.072	0.202	0.332	17.3555	0	0	0
Basak[14]	2.4	−1.2	294.619	693.601	1632.89	0.327022	0.327022	0.327022	3.948	0.57745	1.65	2.369
Yakub[15]	2.2208	−1.1104	187.03	432.18	883.12	0.3422	0.3422	0.3422	3.996	0.5055	1.864	2.378

describe accurately the crystallographic and elastic properties of UO$_2$. The calculations used regular grids of k points with equivalent densities of sampling of the Brillouin zone of the four phases. In practice, the grids were determined by finding the smallest regular grid whose smallest reciprocal vector is at least 3.7 nm long. We have performed DFT-GGA energy minimizations in order to determine the equations of state of the $Fm\bar{3}m$, $Pnma$, $Pbcn$, and $P4_2/mnm$ structures. The calculations at each given volume were done with full relaxation of internal parameters.

Since the main goal of this study is to calculate the relative stability of the different phases as a function of the volume, for simplicity no spin polarization was considered for either $Pnma$, $Pbcn$, or $P4_2/mnm$ phases of UO$_2$. Moreover, the magnetic structures of most of these lattices are not known experimentally, and thus were not taken into account. These problems have been discussed by Geng *et al.* in the case of $Pnma$.[4] However, structural analysis was performed to ensure the validity and the relevance of the resulting configurations.

The result is the description of the energy as a function of the volume for each crystalline structure. We calculate a thermodynamic transition pressure between two phases by calculating a tangent common to both energy curves, and the corresponding volume change. It is known that this method does not give an exact value when an energy barrier exists between the two structures, like in the case of $Fm\bar{3}m$ and $Pnma$.[4] In this case, this thermodynamic transition should be taken as an estimate. This structure has also more issues that will be discussed later.

B. Empirical potentials

In order to assess the empirical potentials, we also calculated the equations of state of each phase with static calculations. The optimization was carried out for each urania structure at given volumes with full relaxation of the angles, the cell, and the internal parameters. We also performed standard MD simulations in the NPT ensemble at very low temperature (10 K) to complete the description of the $Fm\bar{3}m$, $Pnma$, $Pbcn$, and $P4_2/mnm$ urania structures given in Table I.

A large variety of interatomic empirical potentials are available to model UO$_2$. The reviews of Govers *et al.*[22,23] and Potashnikov *et al.*[24] compare most of them in various domains of application but always in the $Fm\bar{3}m$ structure. A recent study done by Chernatynskiy *et al.*[25] has compared 26 interatomic potentials and assessed the structure stability for UO$_2$. However, this study only calculated for each potential the energy of the ground-state structure, but does not describe the equations of state for each phase. Here, in order to describe

in detail the different polymorphs that appear under tensile or compressive load, we have chosen to compare four of the most used potentials: Morelon,[12] Arima,[13] Basak,[14] and Yakub.[15] All of them are based on a rigid ion approximation with only pairwise interactions. The potentials are of similar analytical form, which is composed of a Coulomb term, a Born-Mayer-Huggins like repulsive term, and a van der Waals attractive term for the anion-anion interactions. For two of the potentials (Basak and Yakub) a covalent Morse term for the cation-anion interactions is added. Thus, the general form of the interaction energy between two atoms of chemical species α and β, separated by a distance r, is written as follows:

$$V_{\alpha\beta}(r) = \frac{Q_\alpha Q_\beta}{4\pi\epsilon_0 r} + A_{\alpha\beta}\, e^{-r/\rho_{\alpha\beta}} - \frac{C_{\alpha\beta}}{r^6}$$
$$+ D_{\alpha\beta}[e^{-2B_{\alpha\beta}(r-r_c)} - 2\, e^{-B_{\alpha\beta}(r-r_c)}]. \quad (1)$$

Here Q is the ionic partial charge; $A_{\alpha\beta}$, $\rho_{\alpha\beta}$, $C_{\alpha\beta}$, $D_{\alpha\beta}$, $B_{\alpha\beta}$, and r_c are adjustable parameters. The values of these parameters for all potentials are given in Table II. It should be noted that for the Morelon potential the cation-cation interactions are only described by the Coulomb interactions. Moreover, the anion-anion interaction is unconventional and is defined by intervals as follows:

$$V_{OO}(r) = \frac{Q_O Q_O}{4\pi\epsilon_0 r}$$
$$+ \begin{cases} A_{OO}\, e^{-r/\rho_{OO}}, & 0 < r \leqslant 1.2 \text{ Å}, \\ \text{fifth-order polynomial}, & 1.2 \text{ Å} < r \leqslant 2.1 \text{ Å}, \\ \text{third-order polynomial}, & 2.1 \text{ Å} < r \leqslant 2.6 \text{ Å}, \\ -\frac{C_{OO}}{r^6}, & 2.6 \text{ Å} < r. \end{cases}$$
$$(2)$$

The coefficients of both polynomials are given in Table III. Energy-volume curves obtained with the empirical potentials were used to extract the transition pressures between the phases using the common tangent method.

C. Transition pathways

The use of empirical potentials being far less computationally expensive than the DFT-GGA calculations, we were able to extensively explore the transition pathways between structures under either tensile or compressive load. The aim was to describe the most favorable evolution of the potentially metastable structures with volume changes. In particular, in the tensile domain, the cell parameters have to be carefully controlled to prevent spontaneous recovery to the most thermodynamically stable structure, i.e., the $Fm\bar{3}m$

TABLE III. Polynomial coefficients for the O-O interactions in the Morelon potential.

	Fifth-order polynomial						Third-order polynomial			
	a_0 (eV)	a_1 (eV Å^{-1})	a_2 (eV Å^{-2})	a_3 (eV Å^{-3})	a_4 (eV Å^{-4})	a_5 (eV Å^{-5})	b_0 (eV)	b_1 (eV Å^{-1})	b_2 (eV Å^{-2})	b_3 (eV Å^{-3})
Morelon	479.955	−1372.53	1562.223	−881.968	246.435	−27.245	42.713	−55.29	22.998	−3.1212

structure. In order to achieve this, we have developed a method to closely follow the local energy minima. Contrary to the usual methodology,[26] here no initial pathway deduced from the geometric-topological approach is imposed.

The calculation starts from a known stable configuration, whose domain of stability has been defined from previous investigations of the equations of state (see Sec. IV A). The transition pathways are then determined by following the local minimum energies calculated at different imposed volumes. Each imposed volume is separated by a volume increment δV for which value of 0.5 Å^3 has revealed to be sufficient to smoothly follow the transition paths. At each volume step, the minimum energy of the isovolume hypersurface is extracted from a fine sampling of the cell parameters. In fact, only two (e.g., a and b) of the three lattice axes are imposed. The last one, c, is calculated from the cell parameter-volume relation as follows: $c = V/(a \times b)$. The sampling of the a and b cell parameters was done with windows of ± 0.5 Å by steps of 5×10^{-3} Å. These windows of ± 0.5 Å are sufficient to explore the isovolume hypersurface without having undesired return into the thermodynamically stable $Fm\bar{3}m$ structure. Also, we chose to freeze the angles at their initial values, i.e., 90°, because all the structures studied are either cubic, tetragonal, or orthorhombic. Subsequently, the internal parameters are relaxed by a standard static energy minimization using the GULP code[27] for each (a, b) sampling value. This relaxation enables the determination of the optimized cell and internal parameters at a given constant-volume step. This optimized structure is then introduced as the starting point of the next volume increment, and the constant-volume minimization is repeated until the target volume is reached. This procedure forces the system to stay in local minima along the path, even if these local minima are highly metastable.

In the compressive domain, where urania is found to be the most stable in the $Pnma$ structure, the minimization procedure described above was adapted to explore far larger cell parameter windows. The windows explored at each volume increment were for each free cell parameter equal to ± 2 Å by steps of 5×10^{-3} Å. The exploration of such large cell parameter windows allows us to obtain the transition barrier in the compressive domain, i.e., between $Pnma$ and $Fm\bar{3}m$ structures. However, the method has been deemed unsuccessful for these structure transitions as we will see below.

We also investigated the effects of tensile loads by means of MD simulations in order to investigate the dynamic processes that occur during phase transitions. These calculations were performed at 300 K, with strain rates ranging from 10^7 to 10^9 s^{-1}, along the ⟨100⟩ and ⟨110⟩ directions. These strain rates are many orders of magnitude higher than what occur in reality; nevertheless no significant differences have been found between simulations of different strain rates. Hence, we are

confident the results may be extrapolated to lower strain rates. The size of the simulation box is $8 \times 8 \times 8$ unit cells of the $Fm\bar{3}m$ structure in order to allow long-range effects to happen. At each increment of deformation, the resulting pressure of the simulation box is calculated with the virial theorem and the atomic displacements are recorded. With this procedure one is able to calculate of the pressure-volume curves during phase transition for a given temperature at different strain rates.

IV. RESULTS

A. Equations of state and phase transition pressures

The internal energy versus volume curves and transition pressures for the $Fm\bar{3}m$, $Pnma$, $P4_2/mnm$, and $Pbcn$ phases of UO$_2$ have been calculated with DFT-GGA static energy minimization methods. Note that the equations of state of the $Pnnm$ structure was not considered since this structure could not be stabilized. The results are reported in Fig. 3, with the energies normalized per UO$_2$ formula unit to allow direct comparison of the energy versus volume curves, irrespective of the number of atoms in each conventional cell (see Table I).

As expected, the ground-state structure of urania is the cubic $Fm\bar{3}m$ phase. The equilibrium volume is equal to 39.5 Å^3/UO$_2$ (i.e., 5.4 Å for the unit cell), close to the experimental value of 40.9 Å^3/UO$_2$.[28] At higher pressures,
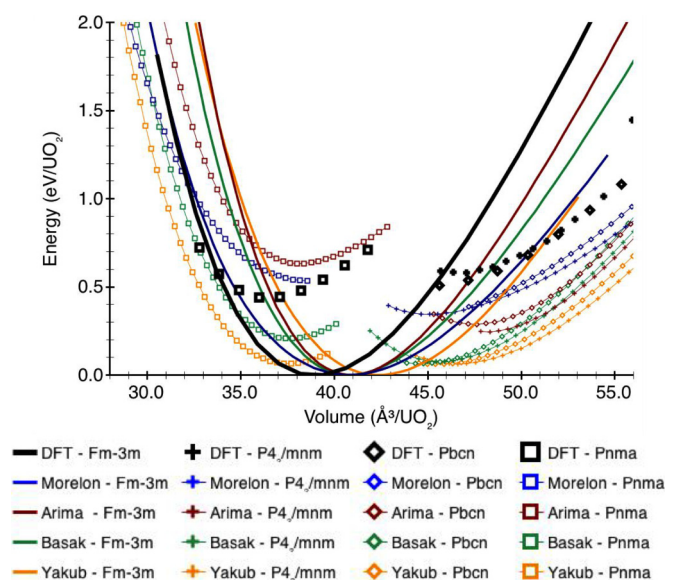

FIG. 3. (Color online) Cell cohesive energy as a function of the cell volume for the $Fm\bar{3}m$ (solid lines), $Pnma$ (squares), $P4_2/mnm$ (crosses), and $Pbcn$ (diamonds) phases calculated with DFT-GGA (black), Morelon (blue), Arima (red), Basak (green), and Yakub (orange) potentials. Both volume and energy are expressed as quantities per UO$_2$ formula.

TABLE IV. Phase transition pressures in UO$_2$ calculated with DFT-GGA and four empirical potentials: Morelon, Arima, Basak, and Yakub. These values are compared with other molecular dynamics simulations and experimental data. We have found only experimental data for the $Fm\bar{3}m$ to $Pnma$ transition. Note that the MD reference value for the $Pbcn$ transition is an estimate.

	This work					Other MD		Exp.	
	DFT	Morelon	Arima	Basak	Yakub	Yu[5]	Desai[7]	Idiri[3]	Benedict[2]
$Fm\bar{3}m \rightarrow Pnma$ (GPa)	28	48	57	10	1.3	20		42	29
$Fm\bar{3}m \rightarrow Pbcn$ (GPa)	−10	−10	−6	−1.7	−1.4		−4.5*		
$Fm\bar{3}m \rightarrow P4_2/mnm$ (GPa)	−11	−9	−5	−1.7	−1.9				

DFT-GGA calculations predict the orthorhombic $Pnma$ phase to be the most stable. The equilibrium volume of the $Pnma$ phase is found around 36.5 Å^3/UO$_2$. This value is close to the one found in previous study with DFT-LSDA+U.[4] For volume greater than 45 Å^3/UO$_2$ (negative pressure), the $Pbcn$ as well as $P4_2/mnm$ phases are more favorable than the $Fm\bar{3}m$ phase. The $Pbcn$ and $P4_2/mnm$ phases are almost energetically degenerate; hence it is impossible to distinguish which phase is the most favorable. The values of the transition pressures between the different phases under tensile and compressive loads are reported in Table IV. The volume differences between each phase for each transition are also reported in Table V. Under compression, DFT-GGA calculations give a transition from the $Fm\bar{3}m$ to the $Pnma$ structure at 28 GPa, with a volume decrease of 7%. This is in agreement with the experimental values of Idiri[3] and Benedict,[2] in which the transition pressure ranges from 29 GPa to more than 69 GPa, with a volume change of 7%. Under tensile load (negative pressure), the transition from the $Fm\bar{3}m$ to the $Pbcn$ or to the $P4_2/mnm$ structure occurs around −10 GPa. These transitions involve large volume expansions of the cells. The volume differences with respect to the $Fm\bar{3}m$ structure are estimated to 21% and 24% increase for the $Pbcn$ and the $P4_2/mnm$ phases, respectively. No experimental data have been found to confirm these values, but it is in qualitative agreement with previous DFT and empirical potential calculations done by Desai *et al.*[7] These authors observed the transitions, but the transition pressures were not quantified. It is worth mentioning that similar pressure-induced phase transitions have been observed in several compounds of type AX_2, where A refers to a cation and X to an anion.[11] For example, PbO$_2$ with the $Pbcn$ structure is known to have a phase transition to the $Fm\bar{3}m$ structure under compressive load.[11] The comparison can also be made with MnF$_2$ in the $P4_2/mnm$ structure. A compressive load on that compound induces a phase transition towards the $Fm\bar{3}m$ structure.[11]

TABLE V. Volume variations of a UO$_2$ cell during the phase transitions calculated with DFT-GGA and four empirical potentials: Morelon, Arima, Basak, and Yakub. All the potentials and the DFT calculations agree qualitatively on the volume variation at the thermodynamic transition.

	DFT	Morelon	Arima	Basak	Yakub	Exp.[3]
$Fm\bar{3}m \rightarrow Pnma$	−7%	−6%	−8%	−8%	−12%	−7%
$Fm\bar{3}m \rightarrow Pbcn$	21%	17%	18%	12%	10%	
$Fm\bar{3}m \rightarrow P4_2/mnm$	24%	15%	20%	9%	8%	

The equations of state of the urania $Fm\bar{3}m$, $Pnma$, $P4_2/mnm$, and $Pbcn$ phases were also calculated with the four chosen empirical potentials. The energies as a function of the volume have been reported on Fig. 3. The transition pressures and volume changes are reported in Tables IV and V, respectively.

Different empirical potentials can give significantly different results as far as the relative energy of different structures is concerned.[25] That said, the four potentials used here predict the correct ground structure, and overall similar behaviors compared to the DFT-GGA calculations. The most favorable phases are, in order from small to large volume, $Pnma$ (high pressure), $Fm\bar{3}m$ (ground state), $Pbcn$, and $P4_2/mnm$ (negative pressure). The latter two curves are very close and hardly distinguishable, with the $P4_2/mnm$ phase slightly lower in energy than $Pbcn$ for the empirical potentials, whereas the opposite is found for DFT calculations. The volume changes (see Table V) calculated by all the empirical potentials are very similar to each other and reproduce fairly well the values obtained by DFT-GGA calculations. However, the phase transition pressures calculated with the empirical potentials show, to some extent, a wide range of values. Basak and Yakub potentials, under tensile load, give smaller transition pressures (around −1 to −2 GPa, respectively) than the DFT-GGA calculations (around −10 GPa). These two potentials also give much lower transition pressures in the compressive domain (10 and 1.3 GPa, respectively) than the experimental value and the DFT-GGA calculations (around 30 GPa). On the other hand, the Arima and Morelon potentials show much better agreement with the experimental and DFT-GGA values. We can note that the Morelon potential exhibits (i) a transition pressure to the $Pnma$ structure in the range of what is observed experimentally and (ii) the transition pressures to the $P4_2/mnm$ or to the $Pbcn$ structure are closer to the DFT-GGA values than with the Arima potential. Therefore, in the following we will show only the results obtained with the Morelon potential. However, most of the studies presented below were also investigated with the three other potentials in order to assess the observed behaviors. For example, we have optimized the four urania phases ($Fm\bar{3}m$, $Pnma$, $P4_2/mnm$, and $Pbcn$) by means of low-temperature (at 10 K) MD simulations at constant pressure (0 GPa) using the four empirical potentials.

The calculated cell parameters and the internal fractional coordinates of each of the four structures are presented in Table I. All four interatomic potentials give similar results. Again, MD simulation of the $Pnnm$ structure was impossible because the structure spontaneously returns to the $Fm\bar{3}m$
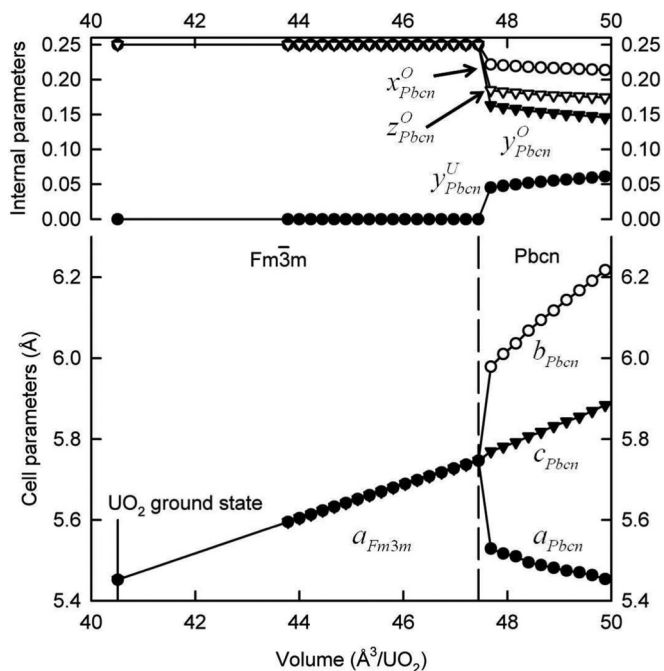
FIG. 4. Evolution of the cell and internal parameters during the $Pbcn$-$Fm\bar{3}m$ transition as a function of volume per UO_2 formula. The a_{Pbcn}, b_{Pbcn}, c_{Pbcn}, and x^O_{Pbcn}, y^O_{Pbcn}, z^O_{Pbcn}, and y^U_{Pbcn} are the cell and internal parameters for the $Pbcn$ structure and a_{Fm3m} refers to the cell parameter of the $Fm\bar{3}m$ structure. The volume of stable urania is indicated by a vertical line and mentioned as the UO_2 ground state. The vertical dashed line marks the volume at the transition point.

structure. The cell and internal parameters reported on the Table I for the $Pnnm$ structure were extracted from the static transformation pathways presented below.

Quantitative variations from one potential to another are to be expected when using classical MD. Moreover, one potential performing well to predict some properties does not imply universal applicability. This is clearly visible here, as the Morelon potential which is the best of the four tested for the transition pressures gives significant lower elastic constants than the others. This is interesting, as it implies that the elastic behavior is not the most important for these phase transitions.

B. Static transformation pathways

Having established the thermodynamic evolution of urania as a function of volume, we investigate the transition pathways from one structure to the next. We recall that we start our calculations from the stable structure of urania and then we smoothly decrease/increase the volume using our energy minimization procedure towards the target volume. Applying a volume decrease (increase of the pressure) from the $P4_2/mnm$ or the $Pbcn$ structure to the $Fm\bar{3}m$ structure we were able to extract the whole transformation pathways. These pathways were analyzed using the FINDSYM software.[29] With this software, we were able to determine the space groups along the transition paths, namely as a function of the volume. We also followed the evolution of the cell and internal parameters as a function of the volume. The results are reported as snapshots
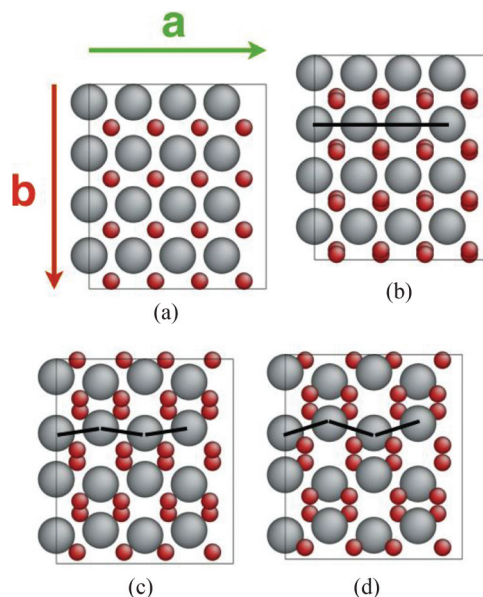

FIG. 5. (Color online) Snapshots of the phase transition from the $Fm\bar{3}m$ to the $Pbcn$ structure projected onto the a-b plane of the $Pbcn$ structure. (a) Crystal in the $Fm\bar{3}m$ structure. The axes correspond to both $Fm\bar{3}m$ and $Pbcn$ settings. (b) The oxygen planes start to glide along the b axis; the uranium ions are still perfectly aligned. (c) The uranium planes begin to glide along the b axis forming a zigzag pattern. (d) Complete transition to the $Pbcn$ structure.

and graphs in Figs. 4 and 5 for the $Pbcn$-$Fm\bar{3}m$ transition and in Figs. 6 and 7 for the $P4_2/mnm$-$Fm\bar{3}m$ transition.

The transition pathway from the urania $Pbcn$ structure down to the $Fm\bar{3}m$ structure is relatively simple from a crystallographic point of view (see Sec. II). Each axis of the $Fm\bar{3}m$ structure corresponds to one axis in the $Pbcn$ structure. The evolution of the cell and internal parameters can then easily be followed (see Fig. 4). Starting from high volumes of around 50 Å^3/UO_2 down to the UO_2 ground-state volume, we observe that urania in the $Pbcn$ structure transits towards the $Fm\bar{3}m$ structure for a volume equal to about 47.5 Å^3/UO_2. From this volume down to the UO_2 ground-state volume (40.5 Å^3/UO_2), urania remains in the $Fm\bar{3}m$ structure. In the $Pbcn$ structure domain, we observe that the b_{Pbcn}-axis length slope is slightly higher than for the two other axes (a_{Pbcn} and c_{Pbcn}) until the transition volume. This b_{Pbcn}-axis length accommodation of the deformation can be seen as well on the evolution of the y^U_{Pbcn} internal coordinate of uranium in the 4c (0, y^U_{Pbcn}, $\frac{1}{4}$) special site. The value of y^U_{Pbcn} smoothly converges down to zero (value for the $Fm\bar{3}m$ structure) at the transition volume. This trend can be visualized in Fig. 5. The zigzag pattern made by the U-U-U chains in the $Pbcn$ structure smoothly aligns along the a axis during the transition to $Fm\bar{3}m$. We also observe change of the positions of the oxygen ions along the b axis. This is related to the strong variations of (i) the y^O_{Pbcn} internal parameter to the value $\frac{1}{4}$ and (ii) the b_{Pbcn} axis length to the $Fm\bar{3}m$ structure value. Close to the transition, we also observe a strong discontinuity of the evolution of the a_{Pbcn}- and b_{Pbcn}-axis lengths. Both shift to one single value by a quasidiscrete step of around 0.2 Å. This discrete transition is also drastic for the internal
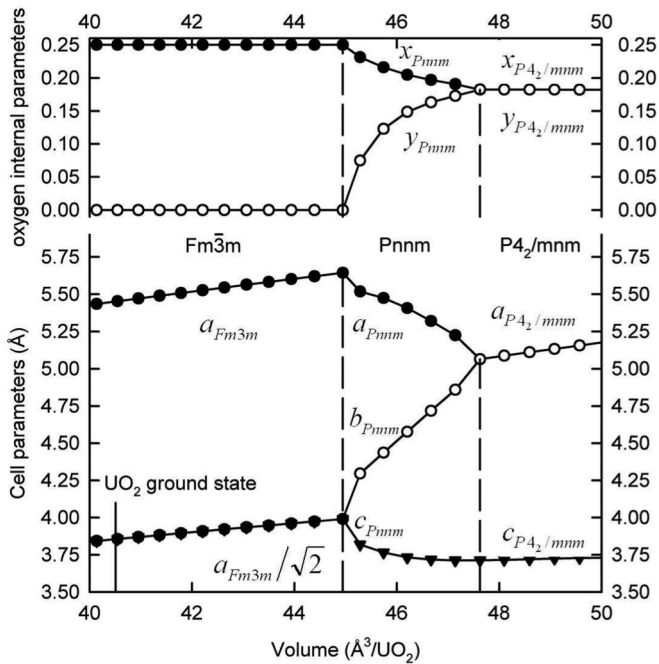
FIG. 6. Evolution of the cell; internal parameters during the $P4_2/mnm$-$Fm\bar{3}m$ transition as a function of volume per UO_2 formula. The $a_{P4_2/mnm}$, $b_{P4_2/mnm}$, $c_{P4_2/mnm}$, and $x_{P4_2/mnm}$, $y_{P4_2/mnm}$ refer to the cell and internal parameters of the $P4_2/mnm$ structure; the a_{Pnnm}, b_{Pnnm}, c_{Pnnm}, and x_{Pnnm}, y_{Pnnm} are the cell and internal parameters of the $Pnnm$ structure; and finally, $a_{Fm\bar{3}m}$ refers to the cell parameter of the $Fm\bar{3}m$ structure. Note that half of the small diagonal $a_{Fm\bar{3}m}/\sqrt{2}$ does appear. In fact, the fluorite conventional cell is expressed in the $P4_2/mnm$ cell, and they are linked to one another by a 45° rotation in the a-b plane. The volume of stable urania is indicated by a vertical line and mentioned as UO_2 ground state. The vertical dashed lines indicate the volume at each transition point.

parameters. These discrete steps are concomitant with the uranium coordination number change from six in the $Pbcn$ structure to eight in the $Fm\bar{3}m$ structure.

The second transition path considered is from the $P4_2/mnm$ to the $Fm\bar{3}m$ structure. The transition is slightly more complicated than the previous one since the pathway contains one intermediate structure. In order to easily follow the transitions, we have reported the evolutions of the cell and internal parameters along the pathway as a function of the volume in Figs. 6 and 7. The transition starts from high volume (50 Å³/UO_2) with urania in the $P4_2/mnm$ structure down to the ground-state structure. We observe along the pathway (see Fig. 6) a first structural transition from the $P4_2/mnm$ structure to the $Pnnm$ structure at about 47.5 Å³/UO_2 and a second structural transition from the $Pnnm$ structure to the $Fm\bar{3}m$ structure at about 45 Å³/UO_2. The system remains in the $Fm\bar{3}m$ structure for smaller volumes down to the UO_2 ground-state volume. In the $P4_2/mnm$ structure domain, only the basal plane axes ($a_{P4_2/mnm} = b_{P4_2/mnm}$) decrease with volume. The oxygen internal parameters start to split smoothly at the transition to the $Pnnm$ structure. This is concomitant with the faster split of the basal plane axes ($a_{P4_2/mnm} = b_{P4_2/mnm}$) of the $P4_2/mnm$ structure to the axes of the $Pnnm$ structure
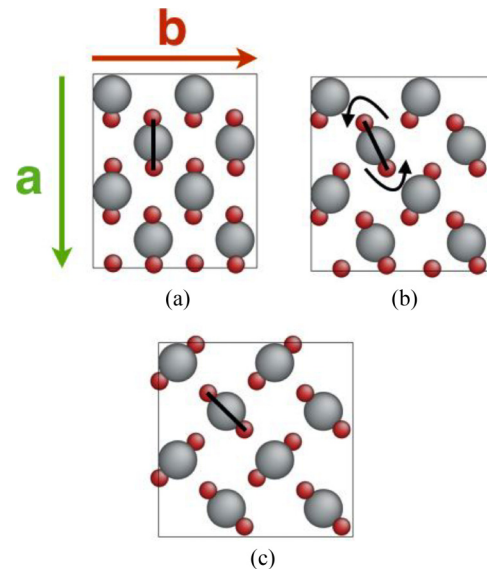

FIG. 7. (Color online) Snapshots of the phase transition from the $Fm\bar{3}m$ to the $P4_2/mnm$ structure projected onto the a-b plane of the $P4_2/mnm$ structure. (a) Crystal in the $Fm\bar{3}m$ structure. The axes correspond to the $P4_2/mnm$ setting. (b) The UO_2 triplets start to rotate. This is the intermediate $Pnnm$ structure. (c) Complete transition to the $P4_2/mnm$ structure. During the transition, the distance between the U ions changes but the other symmetries are not broken whereas the O sublattice is completely reorganized.

($a_{Pnnm} \neq b_{Pnnm}$). Note that the transition from $P4_2/mnm$ to $Pnnm$ structure leaves the c axis almost unchanged, and the evolution from $c_{P4_2/mnm}$- to c_{Pnnm}-axis length remains surprisingly smooth. The $Pnnm$ domain corresponds to the rotation of the UO_6 octahedra around the $c_{P4_2/mnm}$- or the c_{Pnnm}-axis as represented in Fig. 7. The evolution of the cell and internal parameters do have higher amplitudes in the $Pnnm$ structure domain than in the $P4_2/mnm$ structure domain. The b_{Pnnm}- and c_{Pnnm}-axis lengths of the $Pnnm$ structure converge to the $a_F/\sqrt{2}$-axis length of the $Fm\bar{3}m$ structure. This is because the transformation from the $Fm\bar{3}m$ structure to the $Pnnm$ structure involves a 45° rotation of the $Pnnm$ (bc) plane (see Sec. II). The a_{Pnnm}-axis length rapidly converges to the $a_{Fm\bar{3}m}$-axis length of the $Fm\bar{3}m$ structure. The length change of the b_{Pnnm} axis is significant. Its value is reduced by around 1 Å, which corresponds to 20% of its initial value at the $Fm\bar{3}m$-$Pnnm$ transition point. Note that the rapid evolution of the b_{Pnnm}-axis length is somehow compensated by the counteracting change of the y_{Pnnm} internal parameter such that the rotation of the UO_6 octahedra is kept smooth along the transition pathway. The evolution of the c_{Pnnm}-axis length remains small in comparison to the other axes. As observed previously for the $Pbcn$ structure, there is a clear discontinuity of the cell parameters at the transition point from the $Pnnm$ structure to the $Fm\bar{3}m$ structure.

The reverse pathways, i.e., from the $Fm\bar{3}m$ to the $P4_2/mnm$ or the $Pbcn$ structure, were impossible to obtain using our static minimization procedure. However, both pathways could be observed using MD simulations (see Sec. IV C). This impossibility is certainly related to the anisotropic features of the tetragonal $P4_2/mnm$ and the orthorhombic

Pbcn structures. Both require in fact specific anisotropic deformations (see below), along one axis (*Pbcn* structure) or along a linear combination of two axes ($P4_2/mnm$ structure). The transitions are hindered within the static minimization procedure because the three axes of the $Fm\bar{3}m$ structure are strictly equivalent. In practice this means that the deformation of one axis with respect to the others is hardly favored when starting from the highly symmetric $Fm\bar{3}m$ structure.

In the compressive domain, if we start from the *Pnma* structure and apply a volume increase (decrease of pressure), the *Pnma* structure remains stable and never changes to the $Fm\bar{3}m$ structure. Similarly, if we start from the $Fm\bar{3}m$ structure and decrease the volume (pressure increase), the initial $Fm\bar{3}m$ lattice never turns into a *Pnma* structure. Identical behavior was obtained for all the potentials considered herein.

This can be explained by published observations about this transition,[1] which are confirmed with our MD simulations (see below). Indeed, the transition mechanism seems to be at least partially reconstructive, involving the melting of a sublattice. In this case, the simulated system has to be large enough to represent a structure with fewer symmetry elements and possibly a larger unit cell than either the primary and secondary structures. This is consistent with the experiments performed by Idiri[3] in which the transition was observed starting from

42 GPa, although the transition was not complete for all the samples by 69 GPa.

C. Dynamic transformation pathways

The calculation of the static transformation pathways presented above was only possible from high volume structures (*Pbcn* or $P4_2/mnm$) towards the ground-state structure ($Fm\bar{3}m$). Moreover, this procedure leads to discrete step transformation at the transition volume. In order to capture the dynamics and investigate the transitions in both directions, MD simulations at a finite temperature were performed with the Morelon potential by applying uniaxial tensile loading and unloading. The details of the MD simulations are described in Sec. III. Two different uniaxial deformations were applied on urania in the $Fm\bar{3}m$ structure, respectively along the $\langle 100 \rangle$ and the $\langle 110 \rangle$ directions. These directions correspond to the most deformed axes along the static pathways related to both transitions, as can be seen in Figs. 4 and 6.

The pressure-volume curves resulting from these simulations are shown in Figs. 8 and 9. Both figures differ quantitatively, but the overall behavior is the same. At first, the response of the material is elastic, with a small deviation
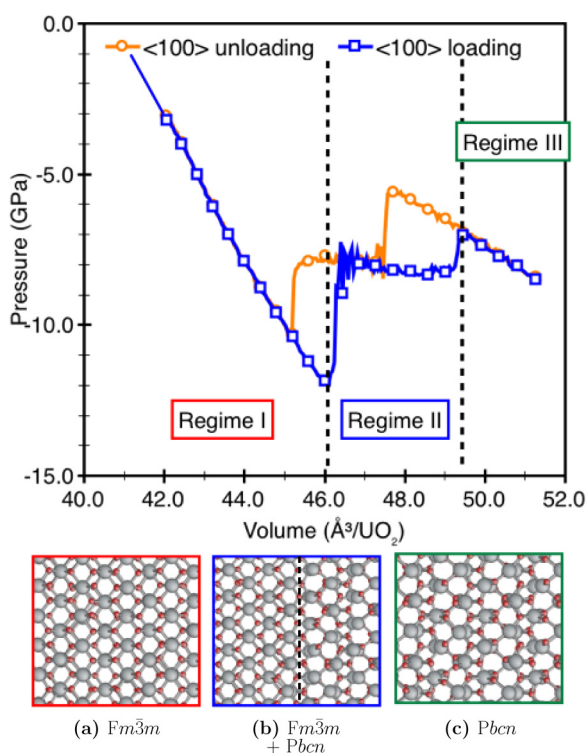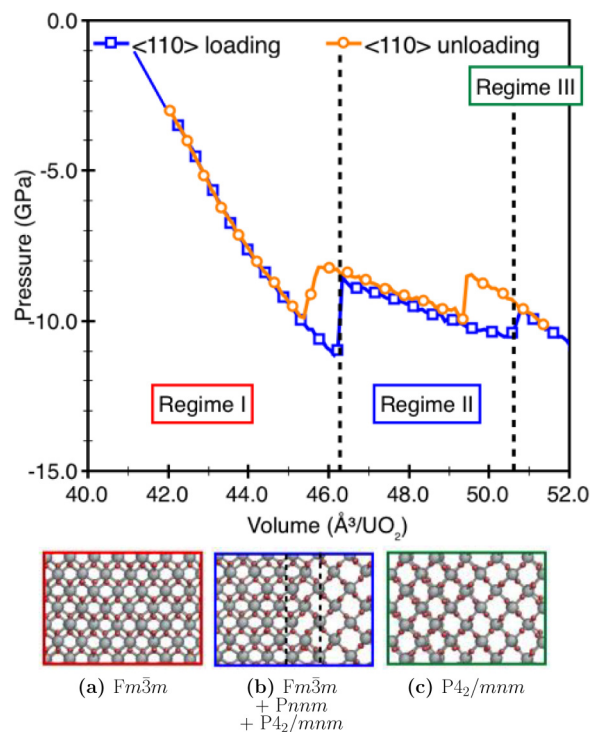

FIG. 8. (Color online) Plot of the pressure as the function of the volume resulting from a uniaxial tensile deformation in the $\langle 100 \rangle$ direction calculated with MD simulation at 300 K. The blue line with square symbols corresponds to the tensile loading and the orange line with sphere symbols corresponds to the unloading. The crystal structures corresponding to each regime are displayed underneath the plot: $Fm\bar{3}m$ structure (regime I), phase coexistence (regime II), and pure *Pbcn* structure (regime III). The interface in the regime II corresponds to the {100} plane of both $Fm\bar{3}m$ and *Pbcn* phases.

FIG. 9. (Color online) Plot of the pressure as the function of the volume resulting from a uniaxial tensile deformation in the $\langle 110 \rangle$ direction calculated with MD simulation at 300 K. The blue line with square symbols corresponds to the tensile loading and the orange line with sphere symbols corresponds to the unloading. The crystal structures corresponding to each regime are displayed underneath the plot: $Fm\bar{3}m$ structure (regime I), phase coexistence (regime II), and pure $P4_2/mnm$ structure (regime III). The interface in the regime II corresponds to the {110} plane of the $Fm\bar{3}m$ phase and the {100} plane of the $P4_2/mnm$ phase.
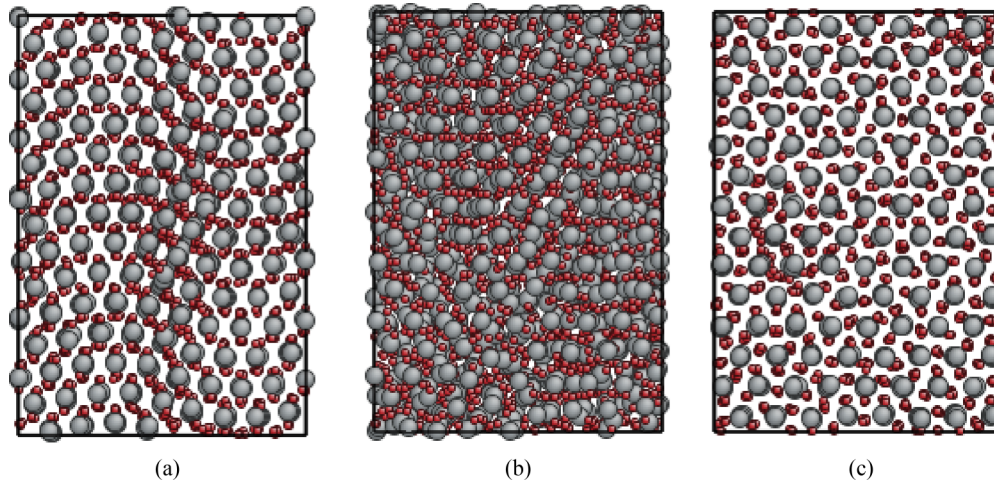
(a)   (b)   (c)

FIG. 10. (Color online) Successive snapshots of a crystal in a $Fm\bar{3}m$ structure, after an uniaxial compression to a pressure of 47 GPa: (a) initial structure showing heavy distortion of its {110} planes and the beginning of a disordered phase; (b) disordered phase occupying the whole simulation box; (c) final structure after a relaxation of 2 ns. The relaxation was a constant volume and at 300 K.

from the perfect linear behavior for deformation in the $\langle 110 \rangle$ direction [regime I, Figs. 8(a) and 9(a)]. At around 46 Å^3/UO$_2$, the negative tensile pressure is the highest and is equal to -12 and -11 GPa for deformation in the $\langle 100 \rangle$ and $\langle 110 \rangle$ directions, respectively. This elastic regime finishes in both cases with an abrupt jump in the pressure, reaching -8 and -8.5 GPa for deformation in the $\langle 100 \rangle$ and $\langle 110 \rangle$ directions, respectively. In the case of the deformation in the $\langle 100 \rangle$ direction, this jump is followed by a plateau until a volume of 49.5 Å^3/UO$_2$, whereas in the case of the deformation in the $\langle 110 \rangle$ direction, the pressure slowly decreases to -10 GPa for a volume of 50.5 Å^3/UO$_2$. After analyzing the structures in this last regime, we found in both cases that it corresponds to the nucleation of secondary phases in the crystal, which coexists with the initial $Fm\bar{3}m$ phase separated with clear interfaces [see Figs. 8(b) and 9(b)]. These phases have been identify as the $Pbcn$ structure for deformation in the $\langle 100 \rangle$ direction and as the $P4_2/mnm$ structure for the deformation in the $\langle 110 \rangle$ direction. Therefore, since both tensile structures are energetically degenerate (see Fig. 3), the deformation direction is crucial to determine which of the two phases will be formed. For this last deformation, we point out that a thin layer of urania in the $Pnnm$ phase is observed between the $Fm\bar{3}m$ and the $P4_2/mnm$ phases. However, this phase is transient and transforms quickly by rotation of the UO$_6$ octahedra to the $P4_2/mnm$ structure as the elongation along the $\langle 110 \rangle$ direction increases as shown in the static transformation pathway in Sec. IV B. The formation of these new phases dissipates some of the internal stresses and causes brutal pressure change for both directions of deformation. After this transition regime at around 49.5 and 50.5 Å^3/UO$_2$ for the $\langle 100 \rangle$ and the $\langle 110 \rangle$ directions, respectively, the systems show again a linear decrease corresponding to the elastic regime of the secondary phases [regime III, Figs. 8(c) and 9(c)]. Beyond a volume of around 52 Å^3/UO$_2$ for both $\langle 100 \rangle$ and $\langle 110 \rangle$ directions, the pressure collapses abruptly due to the rupture of the secondary phases.

It is important to state here that the coexistence of two phases during the transition and the brutal change of the internal parameters shown in Sec. IV B are indicative of a first-order transition. Therefore, the highest negative tensile pressure (-12 and -11 GPA) can be considered as the dynamic transition pressure. These values are in good agreement with the thermodynamic transition pressures calculated from the equations of state. Just before the rupture, both systems are unloaded by reducing the volume with the same strain rate in the same direction as for the tensile load. The results of the unloading trace are displayed in the same figures (Figs. 8 and 9) for direct comparison with the tensile load. First, reverse transformation was possible with this dynamic procedure. Both systems showed again the same three regimes. First, elastic unloading of the secondary phase appears, until a transition point at which the $Fm\bar{3}m$ phase nucleates (regime III). Interestingly, the nucleation of the ground phase during unloading does not occur at the same volume than it appeared during loading: 47.5 instead of 49.5 Å^3/UO$_2$ for the $\langle 100 \rangle$ deformation and 49.5 instead of 50.5 Å^3/UO$_2$ for the $\langle 110 \rangle$ deformation. Therefore, a hysteresis loop clearly appears between regimes II and III. Similar hysteresis appears between regime II and I. However, both phase transformations are completely reversible without any plastic deformation, indicating a perfect reversibility of both transitions.

Compressive tests were also carried out using the same procedure to try to trigger a dynamic transition to a $Pnma$ structure. These tests ran up to a pressure of 100 GPa without showing the transition. However, some simulations showed a different behavior during a relaxation following the compression. The relaxations were done at constant volume to prevent the crystal from simply shrinking to the ground state of the $Fm\bar{3}m$ structure. The temperature was also controlled using a Berendsen thermostat. In these cases, the initial structure was not the most favorable one, as shown previously by the energy-volume relations. The initial structure disappeared after undergoing heavy distortion, leaving a disordered phase (see Fig. 10). This secondary phase started disappearing after about 0.5 ns, replaced by a growing, more ordered phase. After a few nanoseconds of relaxation, the third phase occupied the whole simulation boxes. This phase still contained many
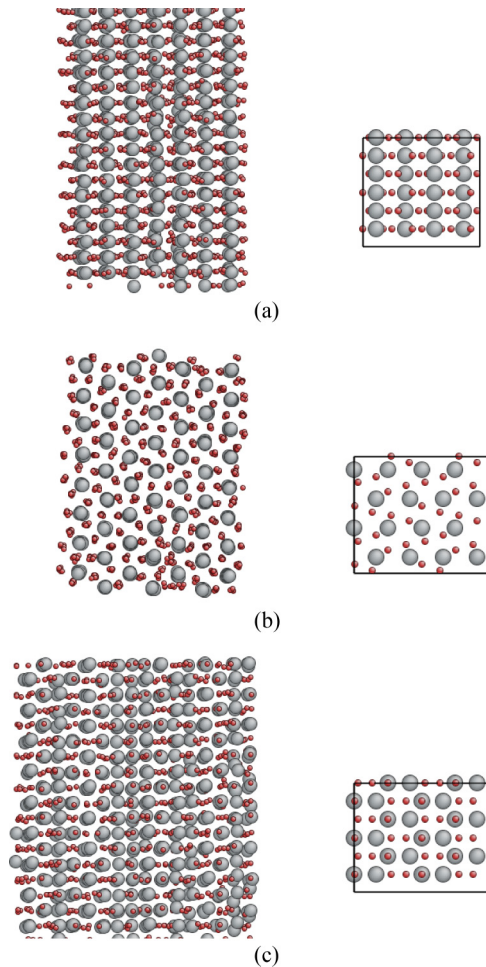
(a)

(b)

(c)

FIG. 11. (Color online) Comparison of the structure obtained after a relaxation at an initial pressure of 47 GPa (on the left) and that of a perfect $Pnma$ crystal (on the right). Some similar features in both configurations are visible, although there are many remaining defects that prevent the formal structure identification.

defects, preventing a formal structure detection to be carried out (like using the FINDSYM code). However, visual examinations showed many symmetry elements similar to those of the $Pnma$ structure, as is shown on Fig. 11. This mechanism is similar to the one previously proposed for the $Fm\bar{3}m$ structure,[1] the main difference being that in our case both sublattices are disordered, whereas the other description involves a disorder mainly contained on the anion sublattice. In our study, uniaxial, biaxial, and hydrostatic compression were tested, but another kind of loading may lead to the transition more easily.

V. CONCLUSIONS

A combination of atomistic simulation methodologies were used to study the relative stability and the transitions between some urania polymorphs under tensile and compressive deformations. Based on previous experimental and theoretical works, we have considered four possible polymorphs: the ground $Fm\bar{3}m$ structure, the high-pressure structure $Pnma$,

as well as the not yet experimentally observed $Pbcn$ and $P4_2/mnm$ structures.

The energy-volume relationships were calculated for these four structures with first-principles calculations using the DFT-GGA approximation as well as with four of the most widely used empirical potentials for UO$_2$ (Morelon, Arima, Basak, and Yakub). The transition pressures were also established from the calculated equations of state. As expected, $Fm\bar{3}m$ is the most stable of the four studied structures under ambient conditions. All the models predicted $Pnma$ to be more stable at lower volumes. The transition between the $Fm\bar{3}m$ and the $Pnma$ structures occurs at 28 GPa, which is in relatively good agreement with the experimental data. In the tensile deformation domain, urania is more stable in either the $Pbcn$ or the $P4_2/mnm$ structure. These two phases are almost energetically degenerate; hence it is impossible to distinguish which phase is the most favorable. For both phases, the transition occurs at around -10 GPa.

From comparison between the four empirical potentials, we have selected the Morelon potential as the most reliable to capture the deformation-induced transitions. It was used to carefully follow the transition pathways between the ground-state and the tensile metastable structures ($P4_2/mnm$ or $Pbcn$), by means of a dedicated static energy minimization procedure. Although all the tested potentials as well as the DTF-GGA calculations give very close transition pressures for $Fm\bar{3}m$-$P4_2/mnm$ and $Fm\bar{3}m$-$Pbcn$ transitions, the transition pathways exhibit very different behaviors. In the case of the $Fm\bar{3}m$-$Pbcn$ transition, there is almost a discrete change for two of the lattice parameters, whereas in the case of the $Fm\bar{3}m$-$P4_2/mnm$ transition, the variation is smoother with an intermediate unstable phase identified as the $Pnnm$ structure.

The static pathways describe the transitions in terms of symmetry and parameter changes, and are not representative of a transition in a large crystal. Indeed, the intermediate states are unstable, and the transition would involve a nucleation and a growth mechanism that should be studied using dynamic methods, rather than a direct transition.

MD simulations were also carried out to capture the dynamics of the $Fm\bar{3}m$-$Pbcn$ and $Fm\bar{3}m$-$P4_2/mnm$ transitions. We discovered that the transition is highly dependent upon the tensile direction: strain in the $\langle 100 \rangle$ direction leads to the $Pbcn$ structure whereas strain in the $\langle 110 \rangle$ direction drives the system to the $P4_2/mnm$ structure. It has been found also that both transitions occur with a two-step mechanism contrary to what has been observed with static calculations. The first step is the creation of an interface between the $Fm\bar{3}m$ and the secondary phases, leading to the coexistence of two or three phases. This step is followed by the complete transformation into the $Pbcn$ or the $P4_2/mnm$ structure according the deformation direction. Similarly to the static pathways, dynamic calculations show a transient $Pnnm$ structure between $Fm\bar{3}m$ and $P4_2/mnm$ structures. These dynamic transitions were completely reversible, showing only a hysteresis loop at the nucleation point of the different phases. Dynamic simulations under compressive loads have shown that the $Fm\bar{3}m$ crystal would turn into a $Pnma$-like structure, but that this involves a transient, high-disorder phase.

---

*p.fossati@imperial.ac.uk

[1] S. E. Boulfelfel, D. Zahn, O. Hochrein, Y. Grin, and S. Leoni, Phys. Rev. B **74**, 094106 (2006).

[2] U. Benedict, J. Alloys Compd. **213**, 153 (1994).

[3] M. Idiri, T. Le Bihan, S. Heathman, and J. Rebizant, Phys. Rev. B **70**, 014113 (2004).

[4] H.Y. Geng, Y. Chen, Y. Kaneta, and M. Kinoshita, Phys. Rev. B **75**, 054111 (2007).

[5] J. Yu, R. Devanathan, and W. B. Weber, J. Phys.: Condens. Matter **21**, 435401 (2009).

[6] T. X. T. Sayle and D. C. Sayle, ACS Nano **4**, 879 (2010).

[7] T. G. Desai and B. P. Uberuaga, Scr. Mater. **60**, 878 (2009).

[8] T. G. Desai, P. Nerikar, and B. P. Uberuaga, Modell. Simul. Mater. Sci. Eng. **17**, 064001 (2009).

[9] Y. Zhang, X.-Y. Liu, P. C. Millett, M. Tonks, D. A. Andersson, and B. Biner, J. Nucl. Mater. **430**, 96 (2012).

[10] P. C. M. Fossati, Ph.D. thesis, École Centrale Paris, Châtenay-Malabry, 2012.

[11] J. M. Léger and J. Haines, Eur. J. Solid State Inorg. Chem. **34**, 785 (1997).

[12] N. D. Morelon, D. Ghaleb, J. M. Delaye, and L. Van Brutzel, Philos. Mag. **83**, 1533 (2003).

[13] T. Arima, S. Yamasaki, Y. Inagaki, and K. Idemitsu, J. Alloys Compd. **400**, 43 (2005).

[14] C. B. Basak, A. K. Sengupta, and H. S. Kamath, J. Alloys Compd. **360**, 210 (2003).

[15] E. Yakub, C. Ronchi, and D. Staicu, J. Chem. Phys. **127**, 094508 (2007).

[16] X. Gonze, B. Amadon, P. M. Anglade, J. M. Beuken, F. Bottin, P. Boulanger, F. Bruneval, D. Caliste, R. Caracas, M. Cote, T. Deutsch, L. Genovese, Ph. Ghosez, M. Giantomassi, S. Goedecker, D. R. Hamann, P. Hermet, F. Jollet, G. Jomard, S. Leroux, M. Mancini, S. Mazevet, M. J. T. Oliveira, G. Onida, Y. Pouillon, T. Rangel, G. M. Rignanese, D. Sangalli, R. Shaltaf, M. Torrent, M. J. Verstraete, G. Zerah, and J. W. Zwanziger, Comput. Phys. Commun. **180**, 2582 (2009).

[17] M. Freyss, T. Petit, and J. P. Crocombette, J. Nucl. Mater. **347**, 44 (2005).

[18] J. P. Perdew, K. Burke, and M. Ernzerhof, Phys. Rev. Lett. **77**, 3865 (1996).

[19] B. Dorado, B. Amadon, M. Freyss, and M. Bertolus, Phys. Rev. B **79**, 235125 (2009).

[20] F. Jollet, G. Jomard, B. Amadon, J. P. Crocombette, and D. Torumba, Phys. Rev. B **80**, 235109 (2009).

[21] B. Meredig, A. Thompson, H. A. Hansen, C. Wolverton, and A. van de Walle, Phys. Rev. B **82**, 195128 (2010).

[22] K. Govers, S. Lemehov, M. Hou, and M. Verwerft, J. Nucl. Mater. **366**, 161 (2007).

[23] K. Govers, S. Lemehov, M. Hou, and M. Verwerft, J. Nucl. Mater. **376**, 66 (2008).

[24] S. I. Potashnikov, A. S. Boyarchenkov, K. A. Nekrasov, and A. Ya. Kupryazhkin, J. Nucl. Mater. **419**, 217 (2011).

[25] A. Chernatynskiy, C. Flint, S. Sinnott, and S. Phillpot, J. Mater. Sci. **47**, 7693 (2012).

[26] D. Zahn and S. Leoni, Z. Kristallogr. **219**, 345 (2004).

[27] J. D. Gale and A. L. Rohl, Mol. Simul. **29**, 291 (2003).

[28] D. G. Martin, J. Nucl. Mater. **152**, 94 (1988).

[29] H. T. Stokes, D. M. Hatch, J. J. Dong, and J. P. Lewis, Phys. Rev. B **69**, 174111 (2004).